AIAA JOURNAL
Vol. 35, No. 6, June 1997

Dynamics of the Vorticity Distribution in Endwall Junctions

C. V. Seal,* C. R. Smith,† and D. Rockwell†
Lehigh University, Bethlehem, Pennsylvania 18015

The dynamics of the vorticity distribution for an unsteady, laminar necklace vortex system are established using quantitative particle image velocimetry techniques. The vortex system is composed of necklace vortices, which form periodically in front of a bluff body junction, translate toward the body, and subsequently amalgamate with a sustained corner vortex. It is shown that cross-diffusion of the necklace vortex vorticity with opposite-sign vorticity generated by a necklace vortex–surface interaction is the dominant mechanism creating a vorticity balance in the system. The instability of the impinging shear layer, under the influence of the adverse pressure gradient generated by the presence of the bluff body, is proposed as the mechanism by which the periodic vortex system frequency is selected.

I. Introduction

THE flow in endwall junction regions is characterized by the formation of necklace (or horseshoe) vortices [i.e., U-shaped vortex tubes with the two legs extending in the downstream direction (Figs. 1 and 2a)], which exhibit a range of behavior depending on Reynolds number. These vortex systems and their potential influence on surface properties such as skin friction have been investigated by several researchers over a number of years.[1–5] Of additional interest has been the impact that the downstream extensions of such vortices can have if they impinge on control surfaces.

Vortex systems formed at the junction of a flat plate and bluff body can be characterized as either laminar or turbulent, depending on the nature of the impinging boundary layer. In the laminar case, recent studies have shown that the boundary layer approaching the bluff body encounters an attachment line upstream of the body,[6–9] where the approaching fluid meets the reverse flow created by the pressure gradient generated by the body. Instead of lifting away from the surface (in a classic separation process), the fluid then flows laterally along the surface and around the sides of the body, forming a shear layer downstream of the attachment line (Figs. 2a and 2b). This is in contrast to the previously accepted belief (and what was reported previously by the authors[10]) that the boundary layer in laminar junction flows undergoes a classical separation. Downstream of this attachment (in the shear layer) the impinging boundary-layer vorticity organizes into the coherent vortices described earlier. The laminar case is characterized by five regimes of behavior[5]: 1) steady—one, two, or three steady-state vortices develop, with the number of vortices increasing with Reynolds number; 2) oscillating—the vortices oscillate periodically with the frequency increasing with Reynolds number; 3) amalgamating—the primary vortex (the vortex closest to the body) breaks away from the formation region and advects toward the body but is subsequently drawn back to and amalgamates with the secondary vortex (the vortex following the primary vortex), forming a new primary vortex; amalgamation is a periodic event for which frequency again increases with Reynolds number; 4) breakaway—the primary vortex periodically breaks away from the formation region and advects downstream toward the body, and the frequency of breakaway increases with increasing Reynolds number; and 5) transitional—the entire vortex system destabilizes into three-dimensional, turbulent-like behavior.

The turbulent case is characterized by the formation of a large-scale, unsteady turbulent vortex upstream of the body, with the position, size, and strength of the vortex varying randomly.[4] In addition, the line of attachment described earlier for the laminar case becomes a line of separation.[8]

The behavior described earlier holds in general for any bluff body–flat plate junction (cylinders, blocks, wedges, airfoils, etc.), provided the presence of the body produces a sufficiently strong adverse pressure gradient.

The objective of the present study was to examine the vorticity distribution and balance in a typical transient vortex system, building on previous work.[10] The present study focuses on the laminar breakaway regime for a flat plate–rectangular block junction, which exhibits organized and periodic vorticity redistribution into discrete vortices, as well as clearly defined vortex–surface interactions. These characteristics are exhibited to some extent in all laminar regimes of behavior and also appear sporadically in the turbulent case. The rectangular block was chosen to increase the size and lateral extent of the necklace vortices, thereby allowing the acquisition of detailed particle image velocimetry (PIV) results.

II. Experimental Apparatus and Methods

Water Channel

Experiments were performed in a Plexiglas® free-surface water channel with a test section 0.3 m deep × 0.9 m wide × 5.0 m long (see Ref. 11 for channel details). A rectangular bluff body [20 cm high × 15.2 cm wide × 5.1 cm deep ($H \times W \times d$)] was located normal to the flow at a distance $L/W = 3.9$ from the leading edge of a flat plate with a 5:1 elliptical leading edge, where L is the distance of the block from the leading edge, and W is the width of the block (Figs. 2 and 3). The freestream velocity was $U_\infty = 50.4$ mm/s, which gave $Re_L = 3 \times 10^4$ and $Re_{\delta*} = 2.98 \times 10^2$ based, respectively, on the distance L and the displacement thickness $\delta*$ calculated for an equivalent flat plate Blasius boundary layer at location L.

PIV

High-image-density PIV[12,13] was used to investigate the velocity field on the symmetry plane. The present study utilized a scanning 8-W laser beam, generated using a rotating polygonal mirror, to illuminate the flowfield. The particle images were recorded on high-resolution film using a 35-mm camera, with image shifting, for later analysis on a personal-computer-based interrogation system, which yields a field of two-dimensional velocity vectors (see Ref. 10 for details). To obtain sufficient spatial resolution, it was necessary to magnify the flowfield, thus allowing a view of only a part of the vortex system at one time. Therefore, two sets of data were obtained with slightly overlapping fields of view to establish collective data covering the whole vortex system (Fig. 3). The first set of experiments[10] covered the translation/amalgamation region (84 × 24 mm) in which the vortices enter the field of view from the left, advect downstream, and amalgamate with a corner vortex (see Sec. III). The second set of experiments focused on the upstream formation region to examine how the impinging boundary-layer

Presented as Paper 95-2238 at the AIAA 26th Fluid Dynamics Conference, San Diego, CA, June 19–22, 1995; received Sept. 16, 1996; revision received Feb. 12, 1997; accepted for publication March 3, 1997.

*Research Assistant, Department of Mechanical Engineering. E-mail: cvs0@lehigh.edu. Student Member AIAA.
†Professor, Department of Mechanical Engineering. Member AIAA.

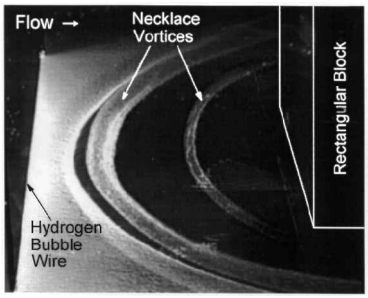

Fig. 1 Hydrogen bubble visualization of an unsteady, laminar necklace vortex system.

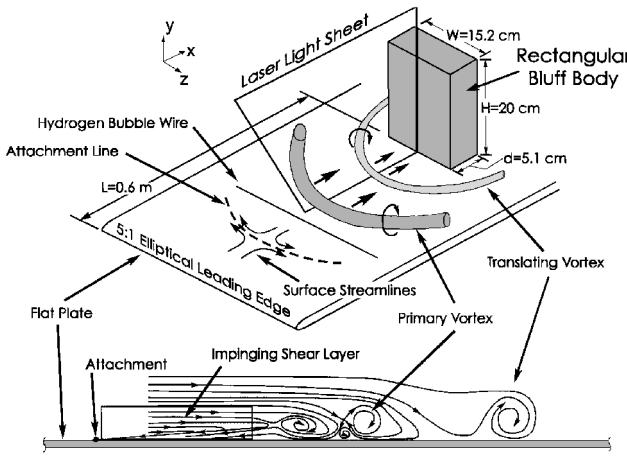

Fig. 2 Schematics of a) laminar necklace vortex system and experimental configuration and b) symmetry plane of the flow topology illustrating the attachments point and the resulting shear layer (adapted from Ref. 6); note that the details of the flow very near the block have been omitted.

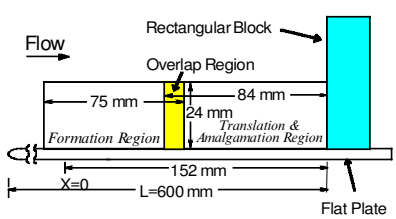

Fig. 3 Schematic of rectangular block mounting and field of view used for the two overlapping sets of PIV experiments.

vorticity is organized into the necklace vortices. Figure 3 shows the physical orientation of the two fields of view. Note that both fields of view are located downstream of the boundary-layer attachment. Data were taken at 1.0-s intervals in the translation/amalgamation region and at 0.5-s intervals in the formation region; phase resolution of the two fields of view was done in postprocessing. In addition, a second set of data of even higher magnification was obtained for the formation region to provide finer spatial resolution.

The PIV images were interrogated using a single-frame autocorrelation technique applied over interrogation windows that measured 1.7 mm square (measured in the physical plane) for the normal field-of-view case and 1.2 mm square (also measured in the physical plane) for a magnified case; the interrogation windows were overlapped 40% for the normal case and 50% for the magnified case. The final results of the PIV interrogation were velocity fields with a resolution of about 1.0 mm between vectors in the physical plane for the two overlapping regions with normal magnification and about 0.6 mm between vectors for the higher magnification case (see Ref. 10 for a detailed description of the PIV interrogation and data analysis process). These velocity data sets were then used to calculate derived results, such as vorticity and streamlines.

There are two major sources of uncertainty of the velocity field determined via PIV. The first is associated with the particle image capturing and interrogation system, which includes errors introduced by the camera optics, particle slip velocity, uncertainties of the laser scan rate, and interrogation method, etc. Landreth et al.[14] demonstrated that a double-pulsed PIV system (which employs essentially identical methods as the PIV system described earlier) obtained data with an associated uncertainty of $\pm 1\%$, and so a similar uncertainty value is to be expected. The second source of uncertainty is created by the image shifting process. The PIV system described earlier employs a rotating (bias) mirror method[15] to uniformly shift the particle images, thus removing directional ambiguity (see Ref. 10 for details), which can introduce significant errors[16] if the magnitude of the mirror rotation (during the camera exposure) is relatively large. However, the PIV systems employed at Lehigh University utilize very small angular displacements of the bias mirror so that, based on the equations given by Oschwald et al.,[16] the uncertainties due to the rotating mirror are on the order of a fraction of a percent. Therefore, a guarded uncertainty value of 2% was assumed for the present data. Using this value for the uncertainty of the velocity data, we calculated the worst case uncertainty of the derived vorticity data to be approximately 3.2%. The influence of velocity uncertainty on calculated streamline patterns was examined by randomly altering each velocity vector in a selected dataset (Fig. 6; $t = 1.0$ s) by ± 0–5%, generating new streamline patterns and comparing them with the streamline patterns of the original data. This was done for several cases, and no qualitative difference in the streamline patterns could be observed; this suggests that the extracted streamline patterns (Sec. III) are accurate reflections of the physical processes and not a manifestation of data uncertainty.

III. Results and Discussion

Vorticity Contours

Figure 4 is a time sequence of vorticity contours on the symmetry plane (for the 1.0-mm resolution cases) covering slightly more than one complete vortex generation/breakaway cycle. The contour levels are ± 1–± 33 s^{-1} in intervals of 2 s^{-1}. Here data sets from the two fields of view (Fig. 3) were phase matched and combined to yield a complete flowfield. In addition, Fig. 4 shows the peak vorticity values associated with the organized vortical structures at each time step. (The location of the vertical bars correspond to the x location of the peak vorticity measurement.)

As the sequence begins, the impinging boundary-layer vorticity (negative, indicated by dashed lines) begins to organize into a primary necklace vortex (at approximately $x/W = 0.3$). As time proceeds, this primary vortex strengthens and advects downstream (at about 16% of the local freestream velocity), assimilating more impinging boundary-layer vorticity. Simultaneously, the vortex begins to interact with the plate surface, generating opposite-sign vorticity via a local vortex-induced pressure gradient effect[17] that manifests itself as a region both directly beneath the vortex and as a growing tongue just trailing the vortex. This eruptive tongue of vorticity increases in strength and penetration into the boundary layer as the primary vortex grows. Eventually, the interaction between the vortex and the surface becomes so strong that this eruption of opposite-sign vorticity effectively severs the primary vortex from the impinging boundary-layer vorticity (at approximately $t = 3.0$ s), allowing the primary vortex to breakaway from the formation region; the newly released vortex accelerates to a velocity of about 30% of the local freestream, becoming a translating vortex ($t = 3.0$–6.0 s). At the point of breakaway, the primary vortex is about 14–15 mm in diameter [based on the extent of the lowest closed vorticity contour (± 1 s^{-1})], approximately 81–87% of the equivalent, unobstructed Blasius boundary-layer thickness at the block location ($x = 0.6$ m).

The newly released translating vortex advects downstream into the junction corner region, where it decelerates to about 17% of the local freestream velocity, and amalgamates with and reinforces a corner vortex ($t = 1.0$–5.0 s). Just before amalgamation, the vortex diameter has decreased to approximately 11–13 mm (64–75% of the equivalent Blasius boundary layer). The reinforced corner vortex then remains in the corner region, awaiting the arrival of a new translating vortex. The repetition frequency of these events for the particular breakaway case examined was 0.2 Hz, yielding a Strouhal number based on block width of 0.605, which is 3.6 times greater

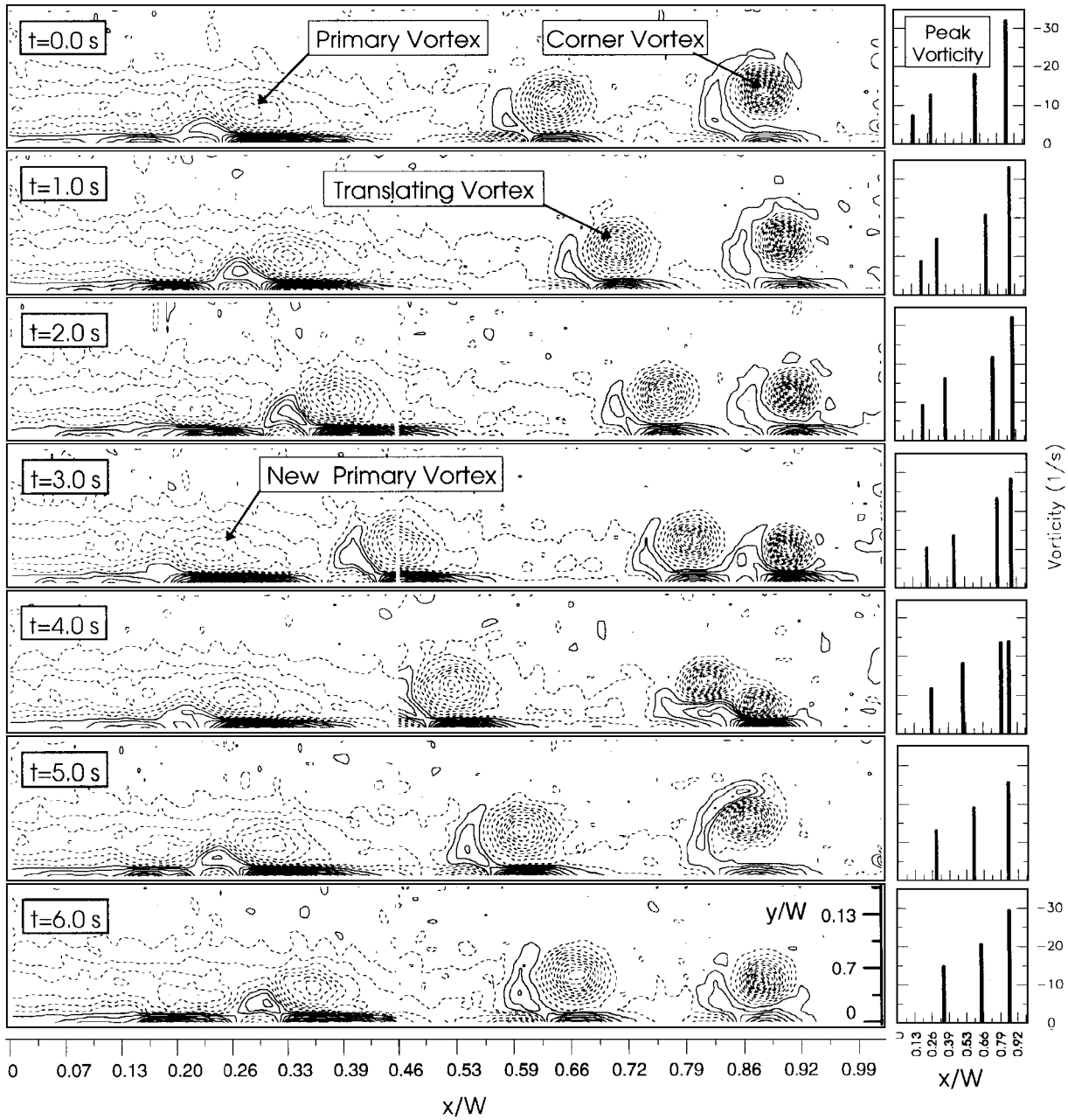

Fig. 4 Vorticity contour and peak vorticity time sequence. Dashed lines indicate negative vorticity, and solid lines indicate positive vorticity. Contour levels range from ± 1 to ± 33 s^{-1} in intervals of 2 s^{-1}. Note that the right-hand sides of the vorticity plots were also presented in Ref. 10.

than the measured wake vortex shedding Strouhal number of 0.17 for the rectangular block.

Plotted adjacent to the vorticity contours in Fig. 4 are values for the peak vorticity associated with both the developing and fully formed necklace vortices; generally, these peak vorticity values occur at the center of the vortical structures. Following the temporal pattern of peak vorticity values illustrates a temporal increase in the vorticity of the primary vortex as it accumulates impinging boundary-layer vorticity. Following breakaway (at about $t = 3.0$ s), the peak vorticity of the primary vortex continually increases, until amalgamation occurs with the corner vortex. This vorticity amplification is presumably due to the stretching of the vortex tube, caused by the three-dimensional deformation of the vortex tube around the sides of the body.

Circulation Strength

Figure 5 plots the nondimensional circulation strength and trajectory of the vortices in the translation and amalgamation region (after breakaway) for the data shown in Fig. 4, as well as for one additional data set at $t = \_1$ s. Circulation was calculated from the velocity data using a line integral:

$$\Gamma_v = \oint \boldsymbol{V} \cdot d\boldsymbol{s} \tag{1}$$

where the integration path was the minimal closed contour of constant negative vorticity ($\omega = \_1$ s^{-1} was taken to be the bounding curve of the vortices); the circulation is nondimensionalized on the equivalent cyclic circulation (Γ_e) calculated by integrating the vorticity flux passing across the upstream edge of the flowfield over one formation breakaway cycle. The circulation behavior was not established for the formation region because the $\omega = \_1$ s^{-1} vorticity contour does not define a clearly closed vortex contour within this region.

Notice that although the peak vorticity values increase following breakaway, the circulation strength of the vortices decreases up to the point of amalgamation. At the point of amalgamation ($t = 4.0$ s), the strength of the corner vortex increases sharply due to the vorticity contributed by the primary vortex. Note that the data points

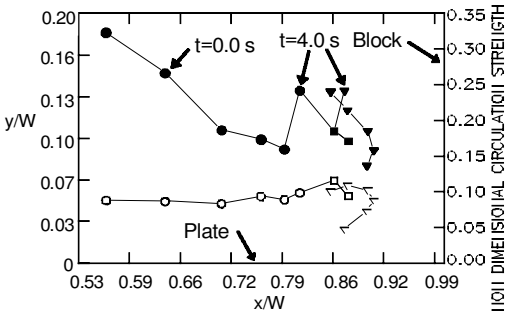

Fig. 5 Vortex trajectory (open symbols) and nondimensional strength (Γ_v/Γ_e, closed symbols), where Γ_e is the time integral of vorticity flux passing across the left edge of the field of view over one cycle. Plotted data correspond to Fig. 4. Circles represent the impinging translating vortex, triangles represent the corner vortex, and squares are the new corner vortex after amalgamation (after Ref. 10).

corresponding to the amalgamating vortices at $t = 4.0$ s in Fig. 5 are indicated by different positions but reflect the same strength for each vortex; this is because the $\omega = \pm 1$ s^{-1} contour (used to define the boundary of a vortex) engirdles both vortices, such that the strength is merged, although at this point the vortices still have distinct centers. Immediately following amalgamation, the new corner vortex rapidly decreases in strength, due to the apparent cross diffusion of vorticity between the necklace vortex and the ejected opposite-sign vorticity generated by the vortex–surface interaction.

This cross-diffusion hypothesis is supported by an examination of the physical processes taking place in the corner region. Note that as the necklace vortices approach the block, they undergo stretching. It is known that during stretching the circulation of an isolated vortex will be conserved in the absence of flux or diffusion of vorticity across a material boundary that initially encompasses all the vortex vorticity. Because the present measurements indicate a substantial decrease in circulation strength, this suggests that viscous effects are responsible for the decrease. There are two ways that viscous effects could come into play. First, vorticity can diffuse across the $\omega = \pm 1$ s^{-1} boundary, and second, the vorticity comprising the vortex could cross diffuse with the corresponding opposite-sign vorticity that is generated at the surface and circulates around the vortex (e.g., see the corner vortex in Fig. 4 for $t = 3.0$ s). The relative importance of these two mechanisms was examined by modeling the necklace vortex as a decaying Oseen vortex matched to the equivalent size and strength of the present vortices; the temporal decay in the strength was then examined (see Ref. 10 for details). The model suggests that pure diffusion processes could only account for a possible 8.0% decrease in circulation strength of the vortex when considered for the period $t = \pm 1.0$–3.0 s, whereas a decrease of approximately 50% was noted for the present study. This suggests that pure diffusion will play only a small part in the noted vortex decay process and that a significant cross diffusion of vorticity must be taking place, leading to a consequent reduction in vortex strength.

Streamline Contours

Instantaneous streamlines for the data corresponding to Fig. 4 were determined (Fig. 6) and topologically assessed using the criteria of Perry and Steiner.[18] The streamline patterns of Fig. 6 illustrate stable foci (the spiraling of streamlines into a central point), which are a known feature of a vortex undergoing stretching (e.g., the sectional streamlines of a Burger's vortex). Also, the streamline patterns of Fig. 6 exhibit several examples of stable limit cycle behavior.[19] For example, in the translation and amalgamation region at $t = 1.0$ s, the translating vortex (labeled T.V.) at the right side of the field of view exhibits a stable limit cycle (i.e., a spiraling inward of external streamlines to a limiting, closed streamline and an outward spiraling of streamlines from the vortex center); simultaneously, the corner vortex (labeled C.V.) displays closed streamlines inside a limiting streamline, suggesting two-dimensional flow. The number of occurrences of closed streamlines is, however, much less than the number of appearances of foci and limit cycles. Limit cycles are also observed occasionally in the formation region, as evidenced

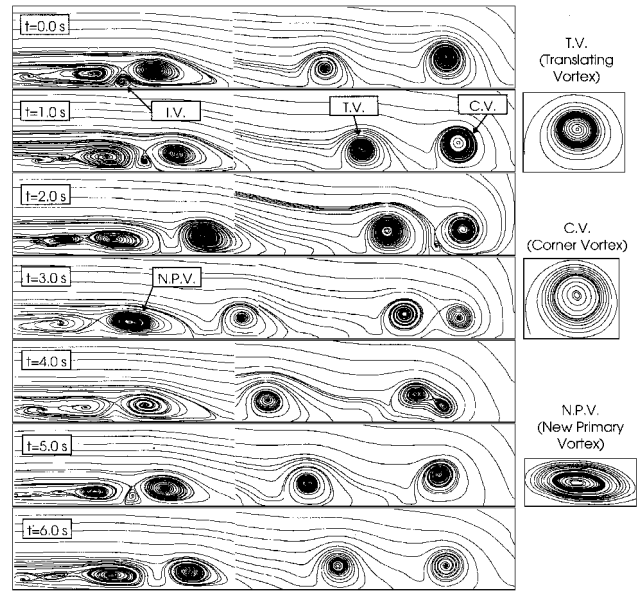

Fig. 6 Instantaneous streamline plots corresponding to Fig. 4. The isolated patterns on the right are expanded views of the labeled vortices in the overall temporal sequence. Note that the right-hand sides of the streamline plots were also presented in Ref. 10.

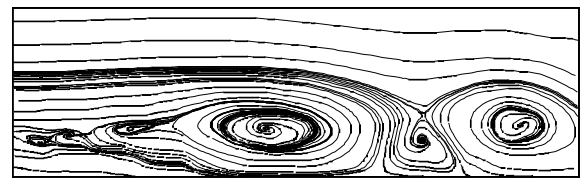

Fig. 7 Streamline plot of magnified case illustrating limit cycles and the modified feeding topology of the induced counter-rotating vortex.

for $t = 3.0$ s, where the new primary vortex (denoted N.P.V.) also exhibits a stable limit cycle. Expanded illustrations of these limit cycle patterns for the particular vortices are plotted at the right side of Fig. 6.

Figure 7 shows a streamline plot for one of the more highly magnified (increased spatial resolution) data fields, roughly corresponding to the formation region of $t = 1.0$ s in Fig. 6; this figure again illustrates the clear presence of limit cycle behavior. The reason for the appearance of limit cycles in the necklace vortices is not immediately clear, but several possibilities exist. First, the necklace vortices may have a two-celled vortex structure like those described by Sullivan,[20] which would display a limit cycle pattern.[18] However, the velocity profiles plotted in Fig. 8, which are representative of the necklace vortices throughout the temporal cycle, display the characteristic shape of only a single-celled structure.[19] In addition, the limit cycles appear intermittently, which suggests some kind of transient phenomenon as the cause of the limit cycle patterns; hence, this two-cell hypothesis seems to be precluded. A more viable possibility may be that the limit cycle patterns are a result of a local deceleration of the axial core flow caused by local, transient, pressure fluctuations along the vortex axis, which could cause a change in the sign of the local gradient, $\partial w/\partial z$, from positive (stretching) to negative (compression). This would be similar to behavior for a leading-edge vortex on a delta wing described by Visbal and Gordnier,[20] who show that the crossflow topology of the vortex can vary, depending on the axial velocity gradient ($\partial w/\partial z$), as well as the ratio of axial to circumferential velocity components. Thus, the appearance of limit cycles in the present results could possibly be explained by continuity considerations (e.g., if the necklace vortex core undergoes stretching, its diameter must decrease, resulting in the observed inward spiraling of streamlines; conversely, compression along the vortex axis will cause expansion of the vortex core, resulting in outward spiraling of streamlines). Clearly, this observed limit cycle behavior requires further investigation to establish its cause.

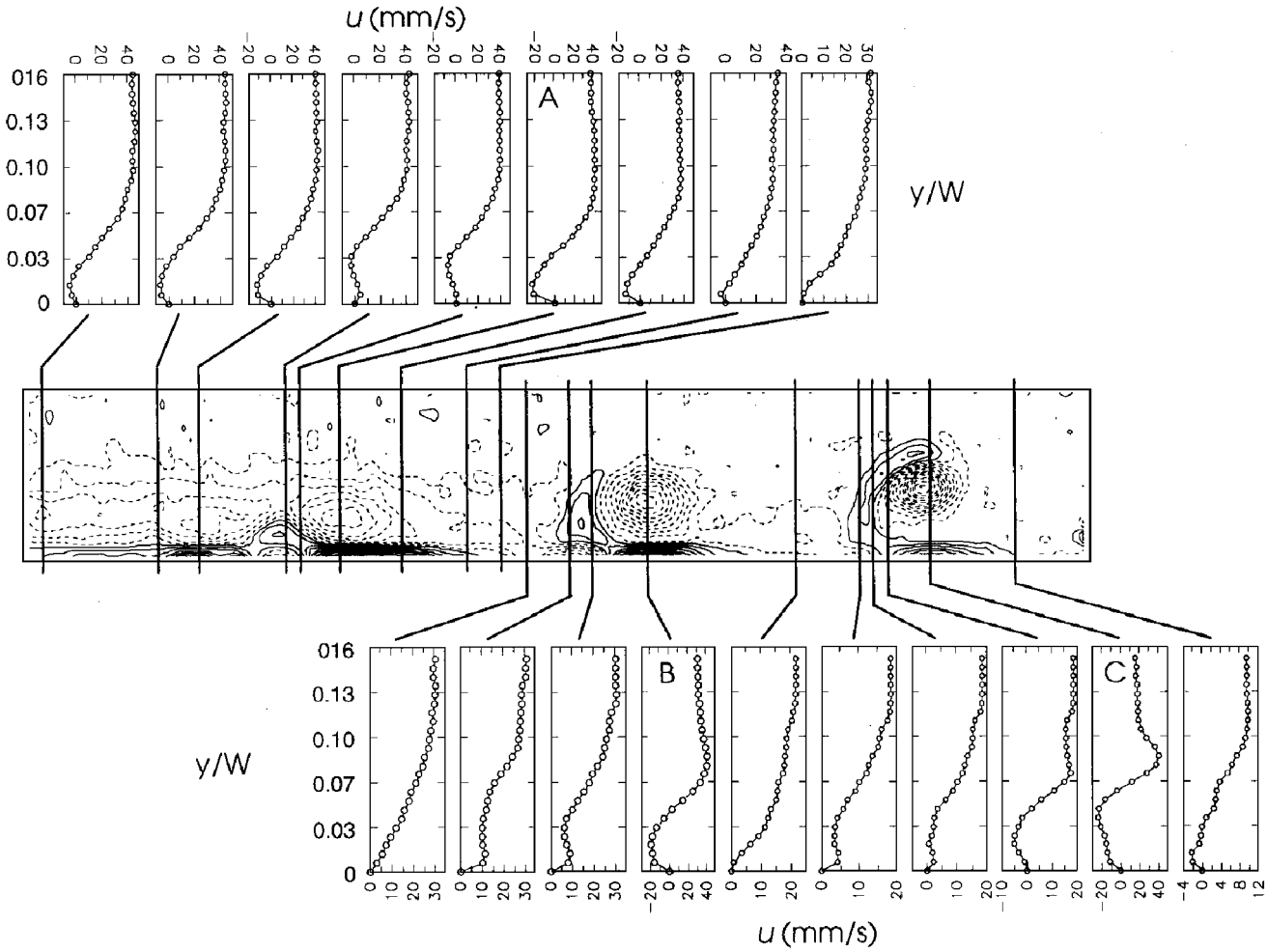

Fig. 8 Selected *u*-velocity profiles for $t = 5.0$ s.

Further examination of Fig. 6 indicates an interesting modification in the topology of the formation region between $t = 0.0$–2.0 s. Beginning at $t = 0.0$ s, the streamlines feeding the induced, counter-rotating vortex (labeled I.V.) in the formation region first pass over the top of the primary vortex (downstream of the I.V.) and then turn upstream to feed the induced vortex. However, by $t = 1.0$ s the streamlines feeding the induced vortex no longer pass around the primary vortex but rather pass over the developing primary vortex (upstream of the I.V.) and then dive, upstream of a saddle point, to feed the induced vortex (also clearly seen in Fig. 7). This temporal change in feeding topology was also found in Visbal's[6] computations of an unsteady laminar juncture flow. This change in topology appears to be associated with the process of primary vortex breakaway. Referring back to Fig. 4, the tongue of opposite-sign vorticity, which extends away from the wall, begins to extend upward at $t = 1.0$ s, initiating a severing of the primary vortex from the formation region, which culminates by $t = 3.0$ s. It is speculated that this change of topology reflects initiation of the vortex severing process that leads to release of the primary vortex.

Velocity Profiles

Figure 8 shows selected *u*-velocity profiles for $t = 5.0$ s, which are very similar to profiles obtained computationally by Visbal for a cylinder–flat plate junction in the laminar breakaway regime. The indication of a reverse wall flow for the most upstream velocity profile suggests that the necklace vortices form well within the region of influence of the adverse pressure gradient produced by the block. Indeed, an examination of the inviscid solution for this type of stagnation flow indicates that the upstream edge of the present field of view is still well within the region of relatively high adverse pressure gradient; the nondimensional pressure gradient is roughly 0.4 at the upstream edge ($x/W = 0$), compared with a peak gradient of 0.9 at approximately $x/W = 0.61$.

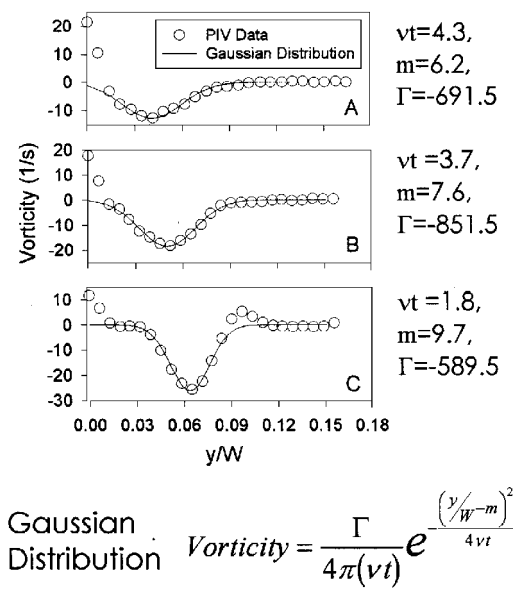

Fig. 9 Wall-normal vorticity distributions (A, B, and C) corresponding to the *u*-velocity profiles labeled A, B, and C, respectively, of Fig. 8.

Figure 8 shows several *u*-velocity distributions for $t = 5.0$ s. Note that velocity profiles of the right-hand sides of $t = 0.0$ and 4.0 s can be found in Ref. 10. From Fig. 8, velocity distributions of the primary and corner vortices appear similar to those of a decaying potential or Lamb–Oseen vortex, with a central core similar to solid body rotation. This observation is supported by Fig. 9, which illustrates favorable comparisons of the wall-normal vorticity distributions of the necklace vortex, in three states development, to fitted

vorticity distributions of a Lamb–Oseen vortex (a Gaussian distribution). Also note the decrease in Γ (the strength of the vortex) from (B) to (C), which matches the behavior of Fig. 5. In addition, the region between the vortices displays Blasius-like behavior, taking on inflectional shapes as the vortex is approached. Peridier et al.[21] showed (in a computational study of a vortex above an infinite plate in the limit $Re \rightarrow \infty$) that pronounced inflectional profiles are a characteristic of vortex-induced boundary-layer separation. The inflectional-shaped profiles observed in the present study are similar (albeit less pronounced due to the relative strength of the vortices) to the profiles computed by Peridier et al.,[21] suggesting the presence of similar local separation processes.

Stability Considerations

Employing the velocity profile results, the stability characteristics of the impinging shear layer were examined to assess a possible relationship to the periodic breakaway frequency of the necklace vortices. Figure 8 suggests the most upstream velocity profile can be approximated as an inflectional mixing-layer profile described by a hyperbolic tangent function. For this shape profile, linear stability theory suggests that the greatest amplification of disturbances occurs for a nondimensional frequency $\omega_\theta \approx 0.21$ (Ref. 22), where

$$\omega_\theta = 4\pi f\theta/\bar{U} \tag{2}$$

and where θ is the momentum thickness, f is the frequency, and $\bar{U}$ is the average velocity of the upper and lower freestream velocities ($U_{\max}$ and $U_{\min}$, respectively) in the shear mixing layer. For the present case, θ was determined as $\theta \approx 1.9$ mm by integration of a typical velocity profile at $x/W = 0.01$ using the standard definition,

$$\theta = \int_0^\delta \frac{|u|}{\bar{U}}\left(1 - \frac{u}{\bar{U}}\right) \mathrm{d}y \tag{3}$$

(note that the $|u|$ term accounts for the effects of reverse flow). The term $\bar{U}$ was approximated by assuming $U_{\max}$ to be equal to the local freestream velocity U (in this case $U \approx 49$ mm s^{-1} at $x/W = 0.01$) and $U_{\min} = 0$. These values indicate a frequency of maximum amplification of $f_{\text{stability}} = 0.22$ Hz, which is very close to the measured frequency of vortex formation and breakaway of $f_{\text{experimental}} = 0.2$ Hz.

Preliminary comparison of the measured frequencies for other breakaway cases (at different Reynolds numbers) suggests a similar consistency with predicted stability frequencies as illustrated in Fig. 10 (open symbols). Since PIV data were not available to determine θ and $U_{\max}$ (at $x/W = 0.01$) for the other cases, θ was approximated using the Blasius formula for a laminar boundary layer, and $U_{\max}$ was determined using an analytical solution for the two-dimensional stagnation flow (in the freestream) around a rectangular body.[23] Although calculating θ via the Blasius equation (and hence for a Blasius boundary-layer profile) is an approximation of the true momentum thickness (of a hyperbolic tangent shaped profile), it is an acceptable one because comparison of a Blasius value with the θ measured from the PIV results indicates a variance of only 5%.

To further examine the possibility of impinging shear layer instability as the mechanism of the necklace formation/breakaway

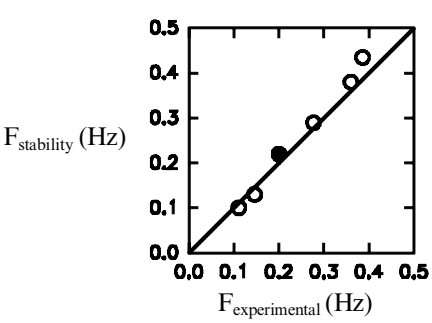

Fig. 10 Comparison of experimentally determined necklace vortex breakaway frequency to frequency predicted using stability concepts. ○ θ calculated assuming Blasius formula and ● θ determined from PIV data.

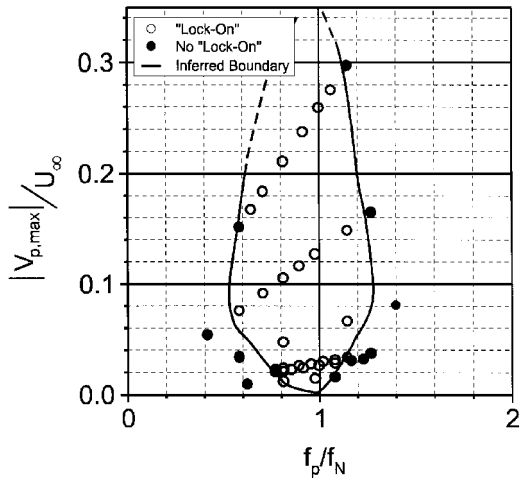

Fig. 11 Experimentally determined map of the lock-on response of an unsteady laminar necklace vortex system in the breakaway regime.

frequency, the response of the laminar unsteady necklace vortex system to applied perturbations was examined. This was done for a circular cylinder–flat plate junction (as part of a more recent study of control of the necklace vortex system). An 8.8-cm-diam (D) cylinder was placed at $L/D = 12.7$ downstream of the plate leading edge with $U_\infty = 8.26$ cm/s, yielding $Re_L = 9.2 \times 10^4$ and $Re_{\delta^*} = 5.25 \times 10^2$ (calculated as described in Sec. II). External perturbations were applied by sinusoidally varying the injection/suction through a transverse surface slot in the flat plate, 63.5 mm transverse by 2 mm wide in the freestream direction over a range of $|V_{p,\max}|$ from 0.0 to 2.5 cm/s, where $|V_{p,\max}|$ is the peak injection/suction velocity over the injection/suction cycle. It was established that within a narrow frequency range (bracketing the natural, unperturbed frequency of 0.48 Hz) the application of local sinusoidal forcing upstream of the attachment line can cause the vortex formation/breakaway frequency to follow the forcing frequency (i.e., lock on to the forcing frequency). However, application of this same type of forcing downstream of the formation region (within the translation region, approximately 0.5 diameters upstream of the cylinder) had no effect on vortex formation/breakaway frequency.

Figure 11 shows a map of lock-on response with the slot located 2.47 diameters upstream of the cylinder, which was upstream of the boundary-layer attachment point. Varying both the frequency and amplitude of the applied perturbations, this map of the region exhibiting a lock-on response was established. The data plotted is nondimensional amplitude ($|V_{p,\max}|/U_\infty$) vs nondimensional frequency (f_p/f_N), where U_∞ is the freestream velocity, f_p is the frequency of the applied perturbations, and f_N is the natural (unperturbed) formation/breakaway frequency. Open symbols denote points where lock-on behavior was observed, and the closed symbols represent the bracketing no lock-on cases. Note that modification of the vortex formation frequency can be influenced by as much as 30–50% for selected injection/suction magnitudes.

In addition, the slot was used to reduce θ in the symmetry plane region by the application of local, constant rate, surface suction upstream of the formation region. Quantification of the reduction in θ was not performed, but hydrogen bubble visualization did reveal an increase in formation/breakaway frequency as the suction was increased (which presumably reduced θ) as Eq. (2) suggests.

The possibility that the formation/breakaway frequency of the vortex system is influenced by downstream conditions of the flow was also examined by comparing the frequency of the vortex formation/breakaway process for the unaltered block with the block retrofitted with a Thwaites-type flap at the trailing edge. To create a Thwaites flap, a 3-mm-thick flat plate that is 3.5 diameters long was placed behind the block on the symmetry plane, which essentially negated the von Kármán shedding behavior of the block. With the flap in place, no change in the necklace formation frequency was observed, suggesting no connection between the necklace vortex formation frequency and downstream conditions. This was also observed in the experiments of Baker.[2]

Taken collectively, these results suggest that the instability of the impinging shear layer is the physical mechanism that determines the frequency of the unsteady necklace vortex system and that downstream influences appear to play no part in the periodicity of unsteady necklace vortex behavior.

IV. Conclusions

An unsteady, laminar necklace vortex system in the breakaway regime was examined quantitatively to establish the vorticity dynamics of the system. From assessment of detailed PIV results, the following can be concluded.

1) The unsteady necklace vortex system exhibits periodic reorganization of impinging boundary-layer vorticity into discrete, translating necklace vortices; the breakaway of these vortices is precipitated by severing the flux of impinging boundary-layer vorticity by ejected opposite-sign vorticity resulting from vortex–surface interactions. These translating vortices ultimately amalgamate with a sustained corner vortex.

2) The necklace vortices display velocity profiles similar to those of an advecting decaying-potential or Lamb–Oseen vortex.

3) On the symmetry plane, the vortex system exhibits both stable foci, which are a characteristic of a vortex subjected to three-dimensional stretching, and stable limit cycle patterns, which are hypothesized to be indicative of local pressure perturbations along the vortex axis.

4) The necklace vortices undergo a systematic reduction in circulation strength due to the cross diffusion of ejected opposite-sign vorticity (generated via vortex–surface interactions) with the necklace vortex vorticity.

5) The instability in the impinging shear layer, formed by attachment of the impinging boundary layer, is the probable mechanism for frequency selection of the periodic breakaway behavior.

6) Utilizing local forcing, the breakaway/formation frequency of the unsteady laminar necklace vortex system may be controlled over a narrow range of frequencies, bracketing the natural frequency.

Acknowledgments

We wish to thank the Air Force Office of Scientific Research (AFOSR) for its support of this research under Contracts AFOSR 49-620-93-1-0217 and AFOSR 49-620-93-1-0346. The continuing support of the AFOSR is gratefully acknowledged. The authors wish to thank J. D. A. Walker and M. Visbal for their advice and assistance. The authors also want to thank D. Rockwell and J. C. Lin for their private communication about uncertainties due to the rotating mirror and M. R. Visbal for sharing velocity profiles obtained computationally.

References

[1]Schwind, R. G., "The Three-Dimensional Boundary Layer Near a Strut," Gas Turbine Lab., Rept. 67, Massachusetts Inst. of Technology, Cambridge, MA, May 1962.

[2]Baker, C. J., "The Laminar Horseshoe Vortex," *Journal of Fluid Mechanics*, Vol. 95, Pt. 2, 1979, pp. 347–367.

[3]Thomas, A. S. W., "The Unsteady Characteristics of Laminar Juncture Flow," *Physics of Fluids*, Vol. 30, No. 2, 1987, pp. 283–285.

[4]Devenport, W. J., and Simpson, R. L., "Time-Dependent Structure in Wing-Body Junction Flows," *Turbulent Shear Flows*, Vol. 6, Springer–Verlag, Berlin, 1989, pp. 222–248.

[5]Greco, J. J., "The Flow Structure in the Vicinity of a Cylinder-Flat Plate Junction: Flow Regimes, Periodicity, and Vortex Interactions," M.S. Thesis, Dept. of Mechanical Engineering and Mechanics, Lehigh Univ., Bethlehem, PA, 1990.

[6]Visbal, M. R., "Structure of Laminar Juncture Flows," *AIAA Journal*, Vol. 29, No. 8, 1991, pp. 1273–1281.

[7]Coon, M. D., and Tobak, M., "Experimental Study of Saddle Point of Attachment in Laminar Juncture Flow," *AIAA Journal*, Vol. 33, No. 12, 1995, pp. 2288–2292.

[8]Hung, C. M., Sung, C. H., and Chen, C. L., "Computation of Saddle Point of Attachment," AIAA Paper 91-1713, June 1991.

[9]Puhak, R. I., Degani, A. T., and Walker, J. D. A., "Unsteady Separation and Heat Transfer Upstream of Obstacles," *Journal of Fluid Mechanics*, Vol. 305, Dec. 1995, pp. 1–27.

[10]Seal, C. V., Smith, C. R., Akin, O., and Rockwell, D., "Quantitative Characteristics of a Laminar Necklace Vortex System at a Rectangular Block-Flat Plate Juncture," *Journal of Fluid Mechanics*, Vol. 286, March 1995, pp. 117–135.

[11]Acalar, M. S., and Smith, C. R., "A Study of Hairpin Vortices in a Laminar Boundary Layer, Part 1. Hairpin Vortices Generated by a Hemisphere Protuberance," *Journal of Fluid Mechanics*, Vol. 175, Feb. 1987, pp. 1–41.

[12]Adrian, R. J., "Particle-Imaging Techniques for Experimental Fluid Mechanics," *Annual Review of Fluid Mechanics*, Vol. 23, 1991, pp. 261–304.

[13]Rockwell, D., Magness, C., Towfighi, J., Akin, O., and Corcoran, T., "High Image-Density Particle Image Velocimetry Using Laser Scanning Techniques," *Experiments in Fluids*, Vol. 14, No. 3, 1993, pp. 181–192.

[14]Landreth, C. C., Adrian, R. J., and Yao, C. S., "Double Pulsed Particle Image Velocimeter with Directional Resolution for Complex Flows," *Experiments in Fluids*, Vol. 6, No. 2, 1988, pp. 119–128.

[15]Adrian, R. J., "Image Shifting Technique to Resolve, Directional Ambiguity in Double-Pulsed Velocimetry," *Applied Optics*, Vol. 25, No. 21, 1986, pp. 3855–3858.

[16]Oschwald, M., Bechle, S., and Welke, S., "Systematic Errors in PIV by Realizing Velocity Offsets with the Rotating Mirror Method," *Experiments in Fluids*, Vol. 18, No. 5, 1995, pp. 329–334.

[17]Doligalski, T. L., Smith, C. R., and Walker, J. D. A., "Vortex Interactions with Walls," *Annual Review of Fluid Mechanics*, Vol. 26, 1994, pp. 573–616.

[18]Perry, A. E., and Steiner, T. R., "Large-Scale Vortex Structures in Turbulent Wakes Behind Bluff Bodies. Part 1. Vortex Formation Processes," *Journal of Fluid Mechanics*, Vol. 174, Jan. 1987, pp. 233–270.

[19]Sullivan, R. D., "A Two-Cell Vortex Solution of the Navier–Stokes Equations," *Journal of the Aero/Space Sciences*, Vol. 26, Nov. 1959, pp. 767, 768.

[20]Visbal, M. R., and Gordnier, R. E., "Crossflow Topology of Vortical Flows," *AIAA Journal*, Vol. 32, No. 5, 1994, pp. 1085–1087.

[21]Peridier, V. J., Smith, F. T., and Walker, J. D. A., "Vortex-Induced Boundary-Layer Separation. Part 1. The Unsteady Limit Problem $Re \rightarrow \infty$," *Journal of Fluid Mechanics*, Vol. 232, Nov. 1991, pp. 99–131.

[22]Monkewitz, P. A., and Huerre, P., "Influence of the Velocity Ratio on the Instability of Mixing Layers," *Physics of Fluids*, Vol. 25, No. 7, 1982, pp. 1137–1143.

[23]Panton, R. L., *Incompressible Flow*, Wiley, New York, 1984, pp. 510–513.

F. W. Chambers
Associate Editor